Applied Physics Express **7**, 055103 (2014)
http://dx.doi.org/10.7567/APEX.7.055103

Short-channel graphene nanoribbon transistors with enhanced symmetry between p- and n-branches

Matthew J. Hollander[1*], Himanshu Madan[1], Nikhil Shukla[1], David A. Snyder[2], Joshua A. Robinson[3], and Suman Datta[1*]

[1]Department of Electrical Engineering, Pennsylvania State University, State College, PA 16801, U.S.A.
[2]Penn State Electro-Optics Center, Pennsylvania State University, State College, PA 16801, U.S.A.
[3]Department of Materials Science and Engineering, Pennsylvania State University, State College, PA 16801, U.S.A.
E-mail: mjh423@psu.edu; sdatta@engr.psu.edu

Received March 12, 2014; accepted March 27, 2014; published online April 30, 2014

Graphene's unique symmetry between p- and n-branches has enabled several interesting device applications; however, short-channel devices often exhibit degraded symmetry. We examine how graphene nanoribbon geometries can improve transfer characteristics and p–n symmetry, as well as reduce Dirac point shift for highly scaled graphene devices. RF graphene transistors utilizing a multiribbon channel are fabricated with channel length down to 100 nm, achieving 4.5-fold improved transconductance, 3-fold improved cutoff frequency, and 2.4-fold improved symmetry compared with sheet devices. The improved performance is linked to reduced contact effects by modeling the extent of charge transfer into the channel as a function of graphene width.

In recent years, significant effort has been made to develop a high-performance graphene-based RF technology that can take advantage of graphene's excellent transport properties and unique characteristics.[1–6] Among these properties, graphene's "V"-shaped transfer characteristic allows for a mixer configuration that utilizes the ambipolar, symmetric nature between p- and n-branches to suppress odd-order harmonics while simultaneously achieving peak conversion gain (CG).[1,2]

While ambipolar mixing was the first configuration to be demonstrated and has since been shown to outperform alternative configurations,[1,2] recent demonstrations have focused predominantly on resistive mixing configurations.[3–6] The shift away from ambipolar configurations can be attributed to degraded transfer characteristics, loss of symmetry between p- and n-branches, and a large shift in V_{Dirac} as channel length (L_{ch}) is scaled to 1 μm and below.[7,8] These effects often make V_{Dirac} inaccessible and lead to degraded CG, making ambipolar configurations infeasible for short-channel devices.

Loss of symmetry and degraded device performance for short-channel graphene field-effect transistors (FETs) are typically attributed to contact effects, which are the result of a screening potential, or charge transfer region (CTR), that exists at the metal-graphene contact as a result of Fermi level pinning at the metal interface.[7–12] In this work, we examine how graphene nanoribbon (GNR) devices can significantly reduce contact effects compared to conventional sheet devices, leading to minimal V_{Dirac} shift and improved symmetry, as well as enhanced on–off ratio and transconductance for graphene devices with L_{ch} as small as 100 nm. Improved performance is attributed to enhanced gate coupling, which works to counteract the negative impact of the CTR. These results highlight the importance of understanding the fundamental electrostatics at play in short-channel graphene sheet and nanoribbon FETs and how they can be controlled to mitigate undesirable effects.

Top-gated GNR structures comprised of single graphene ribbons (50 nm–25 μm wide) with 50-nm-thick HfO_2 gate dielectric (Fig. 1) are prepared along with van der Pauw Hall cross structures ($5 \times 5\,\mu m^2$) and multiribbon GNR RF FETs (10-nm-thick HfO_2 gate dielectric). These devices utilize quasi-free-standing epitaxial graphene (QFEG) that is synthesized on (0001)-oriented, semi-insulating 6H-SiC substrates.[13] GNRs are prepared lithographically, using an oxygen plasma isolation etch to remove unwanted graphene.

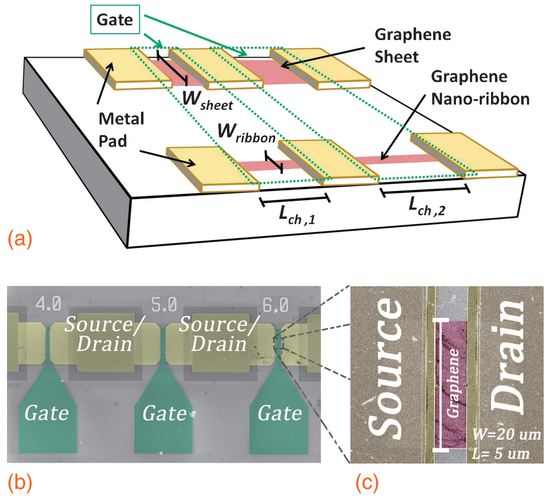

Fig. 1. (a) Schematic representation of sheet and ribbon-based graphene transistors. (b) SEM of final fabricated devices and (c) high-magnification SEM image of graphene channel.

Source/drain contacts (Ti/Au 10/10 nm) are patterned to make direct contact to the GNRs. Gate dielectrics are deposited using e-beam physical vapor deposition (EBPVD) seeded atomic layer deposition (ALD) (2.5 nm HfO_2 seed, 10 or 50 nm ALD HfO_2).[14] Hall effect measurements confirm mobilities as high as 2200 $cm^2\,V^{-1}\,s^{-1}$ at carrier densities of $1 \times 10^{13}\,cm^{-2}$ after dielectric integration.

Figures 2(a) and 2(b) show transfer characteristics for sheet and 50-nm-wide GNR devices as a function of L_{ch} ($V_{ds} = 50\,mV$), indicating that GNR geometries can significantly alter shape, on–off ratio, and degree of symmetry of the transfer curve. For both sheet and GNR devices, a positive shift in V_{Dirac} and quenching of the n-branch are observed and found to worsen as L_{ch} decreases. These trends can be explained by the presence of a p-type CTR near the metal contact, illustrated schematically for the case of long- and short-channel devices in Figs. 2(c)–2(f). By pinning the Fermi level at the metal contact [Figs. 2(e) and 2(f)], the CTR can be viewed as producing a gate-modulated resistance [Figs. 2(g) and 2(h)], which comprises a portion of the device channel. This additional parasitic resistance limits modulation, shifts V_{Dirac}, and contributes to p–n asymmetry through the formation of p–n–p junctions across the device when $V_{gs} > V_{Dirac}$. For long-

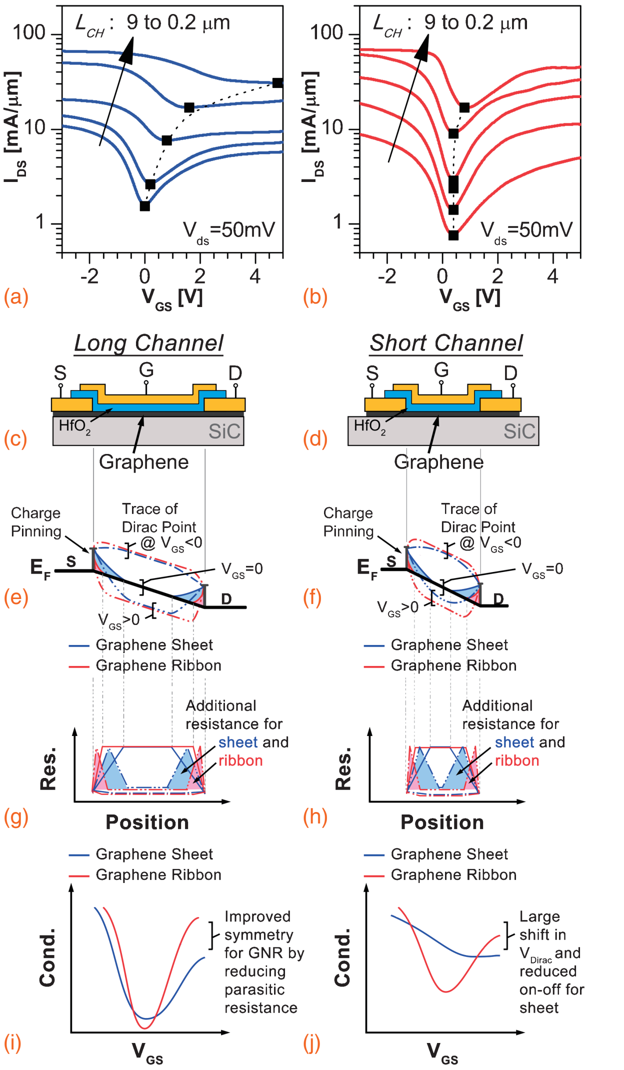

Fig. 2. Family of transfer curves for (a) sheet and (b) 50-nm-wide GNR transistors showing improved symmetry and reduced Dirac shift for GNR devices. Schematic representation of charge transfer phenomenon in (c, e, g, i) long- and (d, f, h, j) short-channel devices showing Dirac shift and quenching of the n-branch (adapted from Ref. 8).

channel devices [Figs. 2(c), 2(e), 2(g), and 2(i)], the CTR comprises only a small portion of the total channel resistance, resulting in minimal quenching of the n-branch and a small shift in V_{Dirac}. For short-channel devices [Figs. 2(d), 2(f), 2(h), and 2(j)], the CTR can extend across a large portion of the device, leading to significant V_{Dirac} shift and quenching of the n-branch, as well as limiting the on–off ratio by lowering the maximum total resistance of the device.

While sheet and GNR geometries show similar trends with decreasing L_{ch}, the extent of Dirac shift and asymmetry is found to depend critically on channel width. Comparing sheet and 50-nm-wide GNR devices for $L_{\mathrm{ch}} = 9\,\mu\mathrm{m}$, we observe Dirac points close to 0 V for both widths; yet as L_{ch} is decreased to 200 nm, sheet devices show a large shift in V_{Dirac} to values >5 V, while GNR devices show significantly reduced V_{Dirac} shift of <1 V. These results can be explained with an effective reduction in CTR length for the GNR geometry [Figs. 2(e)–2(j)]. By reducing CTR length, the additional charge incorporated into the device is minimized and less voltage is required to reach V_{Dirac}. Similarly, the parasitic resistance associated with the CTR can be minimized, yielding improved symmetry and enhanced transfer characteristics.

Although the opening of a transport gap in the range of 10–2.5 meV is likely for the 50-nm-wide GNR, improvement also occurs for the 5- and 1-µm-wide ribbons, where no bandgap is expected. These results are summarized in Fig. 3 along with the results for sheet and 50-nm-wide devices, where a monotonic increase in performance metrics is observed as ribbon width is decreased. Figure 3(a) shows a 3-fold improvement in on–off ratio from 5 to 15 for long-channel devices. Short-channel on–off ratio also improves, although only from 1.5 to 3.5. Similarly, short-channel device transconductance (g_{m}) improves more than 3-fold to $\sim$50 µS/µm with decreasing ribbon width [Fig. 3(b), $V_{\mathrm{ds}} = 50$ mV]; however, we note that the transconductance of the long-channel, 50-nm-wide GNR is significantly degraded compared to other widths. This is attributed to edge roughness scattering for the 50-nm-wide GNR, where additional scattering is expected for GNRs less than 200 nm wide.[15] Furthermore, by moving from sheet to GNR, asymmetry decreases $\sim$2.5-fold from 7.5 to 3 ($L_{\mathrm{ch}} = 0.5\,\mu\mathrm{m}$), where asymmetry is calculated as the ratio of peak g_{m} of the p-branch to peak g_{m} of the n-branch.

The monotonic improvement in transconductance and on–off ratio for graphene ribbons of decreasing width is partially explained by increased fringing fields.[15–17] These fringing fields lead to an increase in capacitive coupling between ribbon and gate, which leads to the accumulation of additional carriers. However, the significant reduction in asymmetry for short-channel devices cannot be explained through increased gate coupling alone. Only by also considering the effect of the CTR and its associated gate-bias-dependent parasitic resistance can we fully explain both the length and width dependencies observed in this work.

Gated TLM measurements provide a direct way of measuring this additional parasitic resistance as a function of gate-bias, where any additional resistance due to the CTR is extracted as part of the contact resistance. Figure 3(d) plots the extracted contact resistance as a function of V_{gs}. For the highly resistive p–n–p biased devices ($V_{\mathrm{gs}} > V_{\mathrm{Dirac}}$), the extracted resistances show a $>$5-fold reduction from $>$2.2 to 0.4 kohm-µm by moving from sheet to 50-nm-wide ribbon geometries. Interestingly, the gated TLM measurements also show a reduction in extracted resistance when $V_{\mathrm{gs}} < V_{\mathrm{Dirac}}$, where no resistive p–n junctions are expected. Furthermore, by moving from sheet to ribbon geometries, we observe a reduction in the anomalous dip in contact resistance at $V_{\mathrm{gs}} = V_{\mathrm{Dirac}}$, which has been linked to the CTR.[18] The 50-nm-wide ribbons exhibit no anomalous dip owing to the mitigated effect of the CTR.

To explain the effect of ribbon geometries in reducing the negative impact of the CTR, the gate–ribbon coupling (C_{gg}) is simulated, and a characteristic length (l_{CTR}) is extracted by fitting the experimental shift in V_{Dirac} with channel length. Figure 4(c) shows V_{Dirac} shift as a function of L_{ch} for graphene devices of various widths and plots the simulated fit. Here, V_{Dirac} shift is given as the difference between V_{Dirac} at a given L_{ch} and V_{Dirac} for $L_{\mathrm{ch}} = 10\,\mu\mathrm{m}$ (long channel). A first-order model of V_{Dirac} shift as a function of L_{ch} is developed to fit the data. In this model, a potential decay from the metal contact into the channel defines the CTR, following Kohmyakov et al.,[11] and the length scale of the decay, l_{CTR}, is used as a fitting parameter.

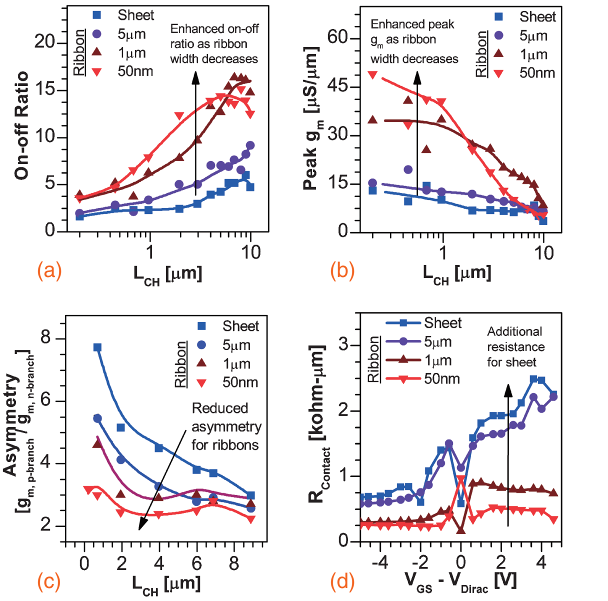

Fig. 3. (a) Enhanced on–off ratio, (b) enhanced peak transconductance, and (c) reduced asymmetry are attributed to a reduction in parasitic resistance associated with the CTR. (d) Gated TLM measurements directly measure this parasitic resistance.

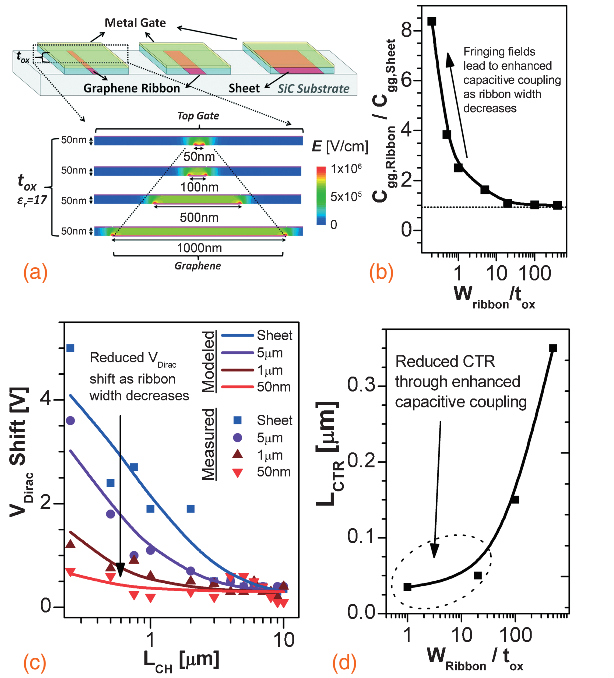

Fig. 4. Simulating capacitive coupling (C_{gg}) between gate and graphene ribbon compared to sheet as a function of ribbon width/t_{ox} (a, b), showing enhanced capacitive coupling due to fringing fields. Experimental and modeled V_{Dirac} shift as a function of channel length (c). Extracted l_{CTR} as a function of ribbon width (d) shows 89% reduction of l_{CTR} from 350 to 40 nm by moving from sheet to 50-nm-wide GNRs.

V_{Dirac} shift is calculated according to $\Delta V_{Dirac} = Q_{CTR}/C_{gg}$, where Q_{CTR} is the additional charge transferred into the device by the CTR and C_{gg} is the simulated capacitance between ribbon and gate [Fig. 4(b)]. These values are extracted from 2D simulations of the metal–oxide–graphene structure [Fig. 4(a)]. Dielectric thickness of 50 nm and dielectric constant of 17 are used. The results confirm a significant increase in capacitive coupling between the graphene channel and metal gate as a result of fringing fields. $C_{gg,ribbon}$ increases 2-fold compared with $C_{gg,sheet}$ as ribbon width is decreased to 50 nm ($W_{ribbon}/t_{ox} = 1$).

Figure 4(d) shows the extracted l_{CTR} as a function of *ribbon width*/t_{ox}. For sheet graphene, an l_{CTR} of 350 nm is extracted. With $l_{CTR} = 350$ nm, the CTR extends more than 800 nm from the metal–graphene interface before reaching equilibrium with the channel. This almost micron-long CTR compares well with recent direct measurements of the CTR on monolayer graphene on bare SiO_2 reported by Nagamura et al., which show the CTR to be on the order of 300–500 nm length, and photocurrent studies of the CTR indicating length scales on the micron order.[9,19] The decay profile and extent of the CTR have been shown to depend on various factors, including the surrounding dielectric environment, extent of Fermi-level pinning, and doping level.[11,12] While it has most often been examined for graphene on SiO_2 without top-gate and never for the case of GNRs, in this work, for the case of QFEG on SiC utilizing a HfO_2 gate dielectric, the extent of the CTR is expected to be significantly increased as compared with that of graphene on SiO_2. This is primarily a result of the increase in effective dielectric constant at the graphene interface from 2.5 to ~13. Constraining the graphene to a 50 nm GNR leads to an 89% reduction in l_{CTR} to 40 nm, which is attributed to enhanced charge control in GNR devices due to fringing fields. Reduction in l_{CTR} extracted from the experimental model of V_{Dirac} shift explains the enhanced on–off ratios and symmetry for GNR devices as a direct result of a reduction in the parasitic resistance incorporated by the CTR.

The effect of GNR geometry on the improvement of C_{gg} and reduction in contact effects is of particular importance for highly scaled graphene transistors. To this end, we design and fabricate two-finger, ground–signal–ground configured RF FETs using multiribbon GNR channels and 10-nm-thick HfO_2 gate dielectric. RF FETs have L_{ch} ranging from 100 nm to 1.3 μm with a device width of 50 μm. The total channel width, W_{ch}, depends on the density and number of GNRs that comprise the channel. GNRs ranging in width from 50 to 100 nm are prepared with spacings ranging from 75 to 100 nm, yielding ribbon densities of 40–50%.

Figures 5(a) and 5(b) show transfer curves of sheet and multiribbon RF GNR FETs with 50-nm-wide ribbons for four different L_{ch}. Just as for single-ribbon devices, enhanced on–off ratio, transconductance, and symmetry are observed for GNRs compared with sheet devices. Similarly, a reduction in V_{Dirac} shift from >2 to ~0.5 V is observed. Figure 5(c) summarizes the improvements in transfer characteristics for multiribbon GNR FETs with 50-, 70-, and 100-nm-wide ribbons relative to sheet-based ones. Figure 5(c) plots peak transconductance of the p-branch versus L_{ch} and shows a monotonic increase in g_m as ribbon width decreases for devices with $L_{ch} = 0.1$, 0.3, and 0.7 μm. Improvements as high as 4.5-fold compared with sheet devices are observed ($L_{ch} = 0.3$ μm). For $L_{ch} > 0.7$ μm, as for the long-channel single-ribbon devices, the sheet device exhibits a higher peak g_m than GNR devices with nanoribbon width ≤100 nm, indicating that nanoribbon widths ≤100 nm lead to enhanced edge scattering and a reduction in mobility relative to sheet devices.

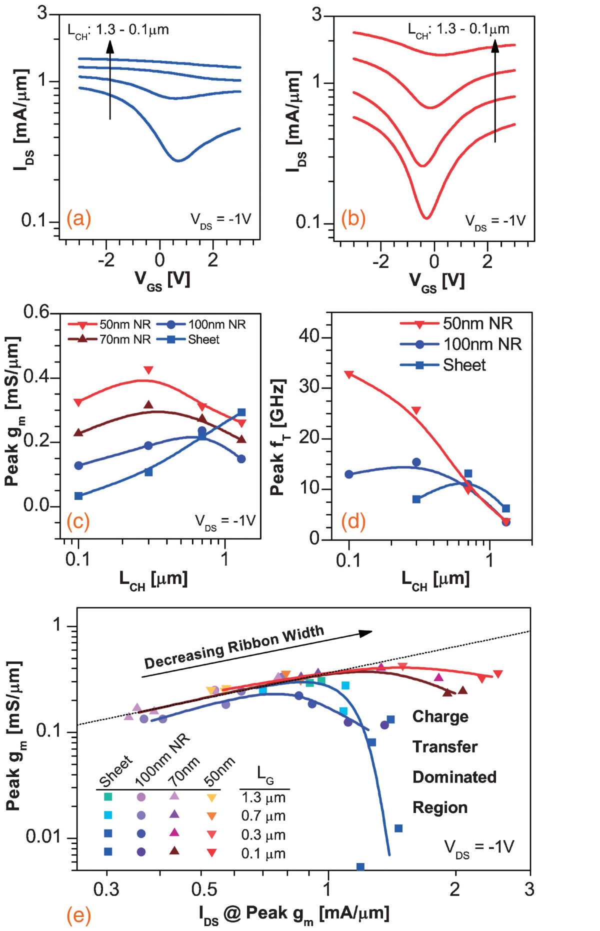

Fig. 5. (a, b) Transfer curves and (c) measured peak g_m for sheet and multichannel GNR RF FETs showing an increase in g_m as ribbon width is decreased. For $L_{ch} = 1.3\,\mu m$, reduced performance compared to sheet is attributed to enhanced edge scattering. (d) Peak f_T versus channel length. (e) Peak transconductance versus drive current shows effectiveness of ribbon geometries in allowing scaling to shorter channel lengths to achieve the highest possible transconductance.

Looking more closely at the variation of g_m with L_{ch}, we see that for sheet devices, peak g_m decreases monotonically as channel length decreases. This degradation in transfer characteristics with decreasing channel length emphasizes the dominance of the CTR at short-channel lengths for sheet-based devices ($l_{CTR} = 350\,nm$). For nanoribbon devices ($l_{CTR} <$ 100 nm), we instead observe an initial increase in peak g_m as L_{ch} is scaled from 1.3 μm down to 300 nm, after which, all three GNR widths show a decrease in peak g_m for $L_{ch} =$ 100 nm, confirming the use of GNR geometries as a technique to reduce l_{CTR} and mitigate the negative impact of the CTR.

RF characterization confirms the benefit of GNR geometries for improving the transfer characteristics of short-channel devices. Comparison of RF performance between sheet and ribbon devices is achieved by extracting the de-embedded current gain cutoff frequency (f_T). Figure 5(d) shows that GNR FETs with $L_{ch} = 300\,nm$ are able to achieve ~3-fold higher f_T than sheet devices, which is attributed to the mitigation of the CTR arising from enhanced gate coupling.

The importance of GNR geometries for highly scaled devices is illustrated by plotting peak transconductance versus drive current [Fig. 5(e)]. In this plot, although increasingly smaller ribbon widths lead to decreased mobility for long-channel devices, they also allow scaling to smaller L_{ch} before the effect of the CTR leads to degraded transfer characteristics. Although mobility is degraded, this ultimately results in higher peak g_m as well as smaller devices. These results are particularly important for ambipolar mixing applications, where high transconductances, short channel lengths, and excellent p–n symmetry are desired.

In conclusion, we have studied how GNR devices can be utilized to reduce contact effects compared with conventional sheet devices. The effect of GNR geometries on the CTR was analyzed by examining changes in contact resistance, symmetry, transconductance, and on–off ratio as functions of ribbon width and length. We experimentally demonstrated the use of ribbon and nanoribbon geometries to enhance gate coupling through fringing fields and reduce the effective length of the CTR. By reducing the impact of the CTR, RF GNR FETs with L_{ch} as small as 100 nm are able to achieve a 4.5-fold improved transconductance, a 3-fold improved current gain cutoff frequency, and a 2.4-fold improved symmetry compared with sheet-based devices. These results highlight the importance of understanding the fundamental electrostatics at play in highly scaled graphene and graphene nanoribbon devices and how they can be controlled to mitigate undesirable effects such as the CTR.

Acknowledgments The authors thank Nidhi Agrawal for help with TCAD simulations. Support for the Cambridge ALD System, LEO 1530 FESEM, and Vistec 5200 was provided by the National Nanotechnology Infrastructure Network at Penn State. This research was sponsored by the Office of Naval Research (Grant N00014-12-C-0124, monitored by Dr. Peter Craig).

1) H. Wang, A. Hsu, J. Wu, J. Kong, and T. Palacios, IEEE Electron Device Lett. **31**, 906 (2010).
2) H. Madan, M. J. Hollander, M. LaBella, R. Cavalero, D. Snyder, J. A. Robinson, and S. Datta, IEDM Tech. Dig., 2012, p. 4.3.1.
3) Y. M. Lin, A. Valdes-Garcia, S. J. Han, D. B. Farmer, I. Meric, Y. Sun, Y. Wu, C. Dimitrakopoulos, A. Grill, P. Avouris, and K. A. Jenkins, Science **332**, 1294 (2011).
4) O. Habibpour, S. Cherednichenko, J. Vukusic, K. Yhland, and J. Stake, IEEE Electron Device Lett. **33**, 71 (2012).
5) J. S. Moon, H. C. Seo, M. Antcliffe, D. Le, C. McQuire, A. Schmitz, L. O. Nyakiti, D. K. Gaskill, P. M. Campbell, K. M. Lee, and P. Asbeck, IEEE Electron Device Lett. **34**, 465 (2013).
6) O. Habibpour, J. Vukusic, and J. Stake, IEEE Trans. Microwave Theory Tech. **61**, 841 (2013).
7) R. Nouchi, T. Saito, and K. Tanigaki, Appl. Phys. Express **4**, 035101 (2011).
8) K. Nagashio and A. Toriumi, Jpn. J. Appl. Phys. **50**, 070108 (2011).
9) T. Mueller, F. Xia, M. Freitag, J. Tsang, and P. Avouris, Phys. Rev. B **79**, 245430 (2009).
10) R. Nouchi and K. Tanigaki, Appl. Phys. Lett. **96**, 253503 (2010).
11) P. A. Khomyakov, A. A. Starikov, G. Brocks, and P. J. Kelly, Phys. Rev. B **82**, 115437 (2010).
12) K. M. Lee, A. Ohoka, and P. M. Asbeck, Int. Semiconductor Device Research Symp., 2011, p. 1.
13) J. A. Robinson, M. J. Hollander, M. LaBella, K. A. Trumbull, R. Cavalero, and D. W. Snyder, Nano Lett. **11**, 3875 (2011).
14) M. J. Hollander, M. LaBella, K. A. Trumbull, R. Cavalero, Z. Hughes, M. Zhu, X. Weng, E. Hwang, D. W. Snyder, S. Datta, and J. A. Robinson, Nano Lett. **11**, 3601 (2011).
15) A. Venugopal, J. Chan, X. Li, C. W. Magnuson, W. P. Kirk, L. Colombo, R. S. Ruoff, and E. M. Vogel, J. Appl. Phys. **109**, 104511 (2011).
16) F. T. Vasko and I. V. Zozoulenko, Appl. Phys. Lett. **97**, 092115 (2010).
17) C. Smith, R. Qaisi, Z. Liu, and M. M. Hussain, ACS Nano **7**, 5818 (2013).
18) R. Nouchi, T. Saito, and K. Tanigaki, J. Appl. Phys. **111**, 084314 (2012).
19) N. Nagamura, K. Horiba, S. Toyoda, S. Kurosumi, T. Shinohara, M. Oshima, H. Fukidome, M. Suemitsu, K. Nagashio, and A. Toriumi, Appl. Phys. Lett. **102**, 241604 (2013).